



# Simultaneous observations of structure function parameter of refractive index using a high-resolution radar and the DataHawk small airborne measurement system

Danny E. Scipi3n<sup>1</sup>, Dale A. Lawrence<sup>2</sup>, Marco A. Milla<sup>1</sup>, Ronald F. Woodman<sup>3</sup>, Diego A. Lume<sup>1</sup>, and Ben B. Balsley<sup>4,†</sup>

<sup>1</sup>Radio Observatorio de Jicamarca, Instituto Geof3sico del Per3, Lima, Peru

<sup>2</sup>Aerospace Engineering Sciences, University of Colorado, Boulder, CO, USA

<sup>3</sup>Instituto Geof3sico del Per3, Lima, Peru

<sup>4</sup>Cooperative Institute for Research in Environment Sciences, University of Colorado, Boulder, CO, USA

<sup>†</sup>deceased, 30 July 2013

Correspondence to: Danny E. Scipi3n (danny.scipion@jro.igp.gob.pe)

Received: 27 October 2015 – Revised: 6 August 2016 – Accepted: 30 August 2016 – Published: 16 September 2016

**Abstract.** The SOUSY (SOUNDing SYstem) radar was relocated to the Jicamarca Radio Observatory (JRO) near Lima, Peru, in 2000, where the radar controller and acquisition system were upgraded with state-of-the-art parts to take full advantage of its potential for high-resolution atmospheric sounding. Due to its broad bandwidth (4 MHz), it is able to characterize clear-air backscattering with high range resolution (37.5 m).

A campaign conducted at JRO in July 2014 aimed to characterize the lower troposphere with a high temporal resolution (8.1 Hz) using the DataHawk (DH) small unmanned aircraft system, which provides in situ atmospheric measurements at scales as small as 1 m in the lower troposphere and can be GPS-guided to obtain measurements within the beam of the radar. This was a unique opportunity to make coincident observations by both systems and to directly compare their in situ and remotely sensed parameters.

Because SOUSY only points vertically, it is only possible to retrieve vertical radar profiles caused by changes in the refractive index within the resolution volume. Turbulent variations due to scattering are described by the structure function parameter of refractive index  $C_n^2$ .

Profiles of  $C_n^2$  from the DH are obtained by combining pressure, temperature, and relative humidity measurements along the helical trajectory and integrated at the same scale as the radar range resolution. Excellent agreement is observed between the  $C_n^2$  estimates obtained from the DH and SOUSY in the overlapping measurement regime from 1200 m up to

4200 m above sea level, and this correspondence provides the first accurate calibration of the SOUSY radar for measuring  $C_n^2$ .

**Keywords.** Meteorology and atmospheric dynamics (instruments and techniques)

## 1 Introduction

Radars have proven to be important tools for investigating dynamic processes of different temporal and spatial scales in the lower and middle atmosphere (e.g., Woodman and Guillen, 1974; R3ster et al., 1986; Luce et al., 2002, 2007). Frequencies ranging from MF (medium frequency – 3 MHz) to UHF (ultrahigh frequency – 3 GHz) are the most common for studying dynamic processes and structures in the neutral atmosphere.

In general, VHF (very high frequency) and UHF stratosphere–troposphere (ST) clear-air radar returns are sensitive to electromagnetic refractive index fluctuations, which depend primarily on variations of the atmospheric parameters temperature ( $T$ ), relative humidity (RH), and pressure ( $P$ ) at Fourier scales of half the radar wavelength (e.g., R3ttger and Larsen, 1990). Radar returns can be due to isotropic fluctuations in  $T$  and RH associated with active turbulent mixing or anisotropic sheets of stable stratification at a scale of several meters (Luce et al., 1995, 2002). Coupled with typical radar vertical resolutions (100–200 m)

that are large compared to the vertical scales of these disparate phenomena, it has been difficult to infer what phenomena the radar returns represent. Frequency-modulated continuous-wave (FM-CW) radars are high-resolution and highly sensitive instruments (Richter, 1969) that allow the study of the fine-structure atmosphere with typical resolution of 1 m but only up to 1–2 km. There have been other studies or campaigns that aim to detect turbulent layers in the troposphere and stratosphere with reasonable resolution: Röttger and Schmidt (1979) used high-resolution pulse scanning to improve the range resolution ( $\sim 30$  m), Cho et al. (1996) detected turbulent layers above the tropopause with a 20 m radar resolution, and Hocking et al. (2014) used digital deconvolution to achieve wind profiler measurements with 60 m resolution

Additional measurements are clearly needed, both at higher resolution and with complementary sensitivities to the phenomena of interest. Hocking and Mu (1997) examined the conversion from structure function parameter of refractive index ( $C_n^2$ ) to kinetic eddy dissipation rates ( $\epsilon$ ) from Buckland Park radar data by using in situ high-resolution thermosonde data ( $\sim 1$  m) to optimize the measurement accuracy.

Other work has compared the backscatter echo received by radar (at 50 m resolution and corrected for range attenuation effects) with the square of the mean vertical gradient of the generalized potential refractive index (obtained from high-resolution radiosonde balloons) (Luce et al., 2002, 2007, and references therein). These have produced excellent correspondence under particular atmospheric conditions with persistent horizontal structure, where the large (many km) separation between an advected balloon and the radar beam are inconsequential.

In the present work, we describe significant improvements in measurement resolution and coincidence between VHF radar returns and in situ measurements in the lower troposphere.

The SOUSY (SOUnding SYstem) VHF radar is a powerful tool with which to study the troposphere and stratosphere (Czechowsky et al., 1976; Röttger and Schmidt, 1979; Ruster et al., 1986), and its observations include wind fields, frontal zones and tropopause height, cumulus convection, gravity wave source mechanisms, and jet-stream-generated dynamic instabilities and turbulence. After its installation at the Jicaroma Radio Observatory (JRO), there have been two main modifications to the SOUSY system (Woodman et al., 2003): first, the antenna size and shape were modified to enable two fixed-beam pointing directions. Second, the control and data acquisition modules were upgraded with a digital receiver system to take full advantage of the wide power-stage bandwidth (4 MHz), resulting in a high spatial resolution (37.5 m).

Coincident in situ measurements of the atmosphere were obtained using a small unmanned aircraft system (sUAS) developed at the University of Colorado, called the DataHawk (Lawrence and Balsley, 2013a). This system consists of a

GPS-controlled, battery-operated aircraft (1 m wingspan), programmed to fly 70 m diameter circles ascending or descending entirely in the radar beam, while measuring temperature, humidity, and winds at 8.1 Hz. Through post-processing of these data, it can also measure  $\epsilon$  (turbulent energy dissipation rate) and structure functions  $C_T^2$  (temperature);  $C_q^2$  (humidity); and, as used here,  $C_n^2$  (refractive index) (Balsley et al., 2012). In order to reach the altitudes above the 1 km radar ground clutter, the DataHawk was dropped from a conventional weather balloon and flown under permission from The Peruvian Corporation of Commercial Airports and Aviation Inc. (CORPAC) air traffic control.

The present work describes the results of this unique coordinated observational campaign where the DH flies on a tight spiral up and down inside the high-resolution SOUSY radar antenna beam over an altitude overlap range of 1.2–4.2 km. This provides the first comparisons using 8.1 Hz colocated in situ measurements of pressure, humidity, and temperature acquired with the DH and scaled to the 37.5 m SOUSY radar resolution. The paper is structured as follows: Sect. 2 describes the theoretical basis for estimating  $C_n^2$  from both in situ DH and radar backscatter measurements. Section 3 provides details on the experimental setup. In Sect. 4, the data collection is described along with the  $C_n^2$  comparison results. Finally, in Sect. 5, conclusions and future work are outlined.

## 2 Theoretical background

In situ and remotely sensed observations are compared on the basis of the structure function parameter of refractive index  $C_n^2$  that is briefly reviewed here. Its estimation from the DH and SOUSY instruments is discussed in separate subsections below.

The energy spectrum of turbulence  $E(\kappa)$  proposed by (Kolmogorov, 1941) can be classified into three regions: the energy-containing range, the inertial subrange (ISR), and the dissipation range. Under this hypothesis, the rate of energy transfer from large scales in the energy-containing range is equivalent to the energy dissipation rate at small scales in the dissipation range (Richardson, 1922). In the inertial subrange, the bulk of energy transfers from larger to smaller scales following a wave number slope of  $-5/3$ . This is also known as the energy cascade assumption or Kolmogorov  $-5/3$  turbulence spectrum for isotropic turbulence, where the turbulence has the same variance in all directions (Tatarskii, 1971). In the troposphere, ISR typically spans large eddy scales of 200 m down to small eddy sizes of 1 cm (Hocking, 1985).

Considering that these turbulent eddies contain air parcels with variations in temperature and humidity, and hence also in the refractive index  $n$ , and assuming that the turbulence is both isotropic and in the inertial subrange,  $C_n^2$  ( $\text{m}^{-2/3}$ ) parameterizes the refractive index structure function  $D_n$  as fol-

lows (Tatarskii, 1971):

$$D_n(\delta) = \langle [n(\mathbf{r} + \delta) - n(\mathbf{r})]^2 \rangle, \quad (1)$$

$$D_n(\delta) = C_n^2(\mathbf{r})|\delta|^{2/3}, \quad (2)$$

$$C_n^2 = \frac{\langle [n(\mathbf{r} + \delta) - n(\mathbf{r})]^2 \rangle}{|\delta|^{2/3}}, \quad (3)$$

where  $\langle \cdot \rangle$  denotes the spatial average over a volume within which the  $n$  irregularities are assumed to be statistically isotropic and homogeneous. Here,  $\mathbf{r}$  represents the position vector,  $\delta$  denotes the spatial separation over which the structure function is being computed, and  $\delta = |\delta|$ .

Estimations of  $C_n^2$  obtained from the DataHawk and the SOUSY radar are detailed in the following subsections. The measured parameters from the DH are obtained at different separations  $\delta$  due to the constant temporal sampling rate, the variable wind speed, and the different vertical ascent and descent rates. Details on the methodology to compare estimates obtained at different turbulent scales (or from DH and SOUSY instruments) are discussed below.

### 2.1 In situ DH measurement of $C_n^2$

If the background atmospheric pressure profile is in hydrostatic balance, then the refractivity  $N = (n - 1) \times 10^6$  can be found directly from the following equations of state (Bean and Dutton, 1966; Rogers and Yau, 1989; Holton, 2004):

$$d \ln P = -\frac{g}{RT} dz, \quad (4)$$

$$e_s = 6.112 \exp\left(\frac{17.6T}{T + 243.5}\right), \quad (5)$$

$$e = \frac{RH e_s}{100}, \quad (6)$$

$$N = \frac{77.6}{T + 273.11} \left( P + \frac{4811e}{T + 273.11} \right), \quad (7)$$

where  $P$  is total atmospheric pressure (hPa),  $e_s$  is the saturated vapor pressure (hPa), RH is the relative humidity (%),  $e$  is the partial pressure of water vapor (hPa),  $P_0$  represents the pressure at  $z = 0$  m (1000 hPa),  $g$  is the gravitational acceleration ( $9.81 \text{ m s}^{-2}$ ),  $R$  is the gas constant for dry air ( $287 \text{ J kg}^{-1} \text{ K}^{-1}$ ), and  $T$  is the temperature ( $^{\circ}\text{C}$ ). The electron density term has been omitted in Eq. (7) due to its influence being only in the ionosphere.

The DH provides in situ measurements of  $P$ ,  $e$ , and  $T$  at 8.1 Hz. With a vertical ascent rate of  $1.0 \text{ m s}^{-1}$  and descent rate of  $2.0 \text{ m s}^{-1}$ , refractivity  $N$  (or equivalently refractive index  $n$ ) can be estimated along the helical path at each of the measured points.

The structure function parameter  $C_n^2$  can be estimated at separation  $\delta$  along the helix path (see black points and solid black line in Fig. 8) using Eq. (3). From now on, this method will be called ‘‘DH direct’’. However, as stated by Wainwright et al. (2015) and Bonin et al. (2015), it is important to account for the advection of turbulence past the DH platform.

To account for this, Taylor’s hypothesis of frozen turbulence is utilized (Taylor, 1938). So, instead of calculating  $\delta$  as the separation of two measurement locations, an effective separation distance  $\delta_E$ , which considers the advection of frozen turbulence, can be defined as

$$\Delta t = t_j - t_i, \quad (8)$$

$$\Delta x = x_j - x_i - u \Delta t, \quad (9)$$

$$\Delta y = y_j - y_i - v \Delta t, \quad (10)$$

$$\Delta z = z_j - z_i - w \Delta t, \quad (11)$$

$$\delta_E = \sqrt{\Delta x^2 + \Delta y^2 + \Delta z^2}, \quad (12)$$

where  $x$ ,  $y$ , and  $z$  are the zonal, meridional, and vertical separation distances between the  $i$  and  $j$  measurements, respectively;  $u$ ,  $v$ , and  $w$  are zonal, meridional, and vertical wind, respectively; and  $\Delta t$  is the time between measurements. Estimates of measured  $n$  are obtained at each irregular separation (black dots in Fig. 8) and then resampled at the desired uniform separation  $\delta_E$  to obtain  $C_n^2$  by interpolating using the six closest points. For comparisons with the SOUSY radar,  $C_n^2$  estimations from the DH must be at the radar Bragg scale  $\delta_E \approx 2.8 \text{ m}$  @ 53.5 MHz as follows (Scipi3n et al., 2008):

$$C_n^2 = \frac{(\Delta n)^2}{\delta_E^{2/3}}, \quad (13)$$

where  $\Delta n$  represents the refractive index difference over the Bragg scale  $\delta_E$ .

Another approach for calculating  $C_n^2$  is adapted from the work of Wainwright et al. (2015) and Bonin et al. (2015), where estimates of the structure function parameters are calculated from circular trajectories at constant heights to account for horizontal variations of  $n$ . Here, estimates of  $(\Delta n)^2$  are calculated for a set of possible separations  $\delta_E$  in each turn of the helical trajectory (shown by different colored lines in Fig 8); then these estimates are separated into  $\delta_E$  length bins to estimate  $D_n = \overline{(\Delta n)^2}$ . Finally,  $C_n^2$  and the ISR are estimated, where  $C_n^2$  is constant and independent of  $\delta_E$ , at the average altitude of that turn. Direct use of this method may not be suitable for the helical patterns, because it highly depends on the ascent and descent rate, and on the vertical variations of  $n$  over one helix turn. In the end, these variations cause a bias in the estimates  $D_n$  that needs to be accounted for. A solution to remove the bias in  $\Delta n$  and thereby improve the estimate of  $D_n$  is to calculate  $D_n$  as the variance of  $\Delta n$  at each 10 m bin. This modified approach will be referred to as ‘‘DH ISR’’.

### 2.2 SOUSY radar measurement of $C_n^2$

Radars transmit pulses at high power in order to maintain the required sensitivity to detect reflections from weak targets at a desired maximum range. The radar equation is used to determine the returned power  $P_r$  based on multiple parameters from a single target with backscattered cross section  $\sigma_b$

(Skolnik, 1990; Doviak and Zrnić, 1993).

$$P_r = \frac{P_{\text{avg}} G^2 \lambda^2 \sigma_b f^4(\theta, \phi)}{(4\pi)^3 r^4 l^2} \quad (14)$$

Here  $P_{\text{avg}}$  is the averaged transmitted power,  $G^2$  represents the gain of the combined transmitting and receiving antennas for the monostatic case, and  $\lambda$  is the radar wavelength. The range to the target is  $r$ ,  $l$  represents the attenuation losses, and  $f^4(\theta, \phi)$  is the two-way normalized power density pattern. The radar equation for a volume filled with targets (Doviak and Zrnić, 1993; Cohn, 1995; Hocking, 1985, 1996; White, 1997) is more appropriate for atmospheric scattering:

$$P_r = \frac{P_t d G^2 \lambda^2}{(4\pi)^3 r_0^2 l^2} \times \frac{c \tau_w}{2} \times \frac{\pi \theta_1^2}{8 \ln 2} \times \eta, \quad (15)$$

where  $P_{\text{avg}} = P_t \times d$ ,  $P_t$  is the peak transmitted power,  $d$  is the duty cycle, and  $r_0$  is the range to the center of the resolution volume. The radar resolution volume size is the minimum separation between two volume targets that permits them to be distinguished by a radar. The second term on the right-hand side of the equation represents the range resolution  $\Delta r = c \tau_w / 2$ , where  $\tau_w$  is the transmitting pulse width. The third term on the right-hand side represents the transmitting beamwidth, where  $\theta_1$  is the 3 dB width (in radians) of the one-way pattern (Doviak and Zrnić, 1993). Finally, the radar reflectivity  $\eta$ , or average backscatter cross section per unit volume (Ottersten, 1969b, c; White, 1997), is a measurement of the radar scattering intensity in units of  $\text{m}^{-1}$ .

The radar reflectivity for clear-air radars is a measure of the scattering intensity caused by refractive index fluctuations present in the radar resolution volume. If the radar half-wavelength (Bragg scale  $\lambda_B = \lambda/2$ ) lies within the inertial subrange, the radar reflectivity can be represented as (Tatarskii, 1961; Ottersten, 1969a; Cohn, 1995; Doviak and Zrnić, 1993; White, 1997)

$$\eta = 0.379 C_n^2 \lambda^{-1/3}. \quad (16)$$

The received radar power  $P_r$  is proportional to the radar reflectivity  $\eta$ , which is a measure of the radar scattering intensity (see Eq. 15). Also,  $\eta$  is proportional to  $C_n^2$  (see Eq. 16). If the radar is calibrated,  $C_n^2$  can be obtained by the above from measurements of return power at every radar dwell time (at the sampling volume resolution  $\Delta r = 37.5$  m).

Unfortunately, an accurate radar calibration can be complex, requiring detailed measurements of the various radar parameters (see Eq. 15), such as the transmitted peak power  $P_t$ , duty cycle  $d$ , antenna gain  $G$ , antenna efficiency, and radar beamwidth  $\theta_1$ , among others. After combining Eqs. (15) and (16), and grouping all the radar parameters that are hard to measure or quantify in a calibration constant  $C$ , a simplified equation for the estimation of  $C_n^2$  can be expressed as

$$\log C_n^2 = \log(P_r \times r_0^2) - \log d - \log \tau_w + C, \quad (17)$$

where  $P_r \times r_0^2$  represents the total range-corrected power.

Estimates of  $C_n^2$  from the DH and the SOUSY radar have been calculated at two different scales: the Bragg scale (2.8 m) and the radar range resolution (37.5 m). From radar theory, the received power is due to the convolution of the eddies within the radar resolution volume with the range-weighting function (e.g., Röttger and Schmidt, 1979; Doviak and Zrnić, 1984). A similar analogy can be applied to the  $C_n^2$  estimates obtained from the DH for fair comparison between the two instruments, which is an approximation of the convolution for Gaussian pulses:

$$C_n^2 = \frac{1}{M} \sum_{m=1}^M C_n^{2(m)} \times W_r^{(m)}, \quad (18)$$

where  $m$  indexes the contribution of each individual eddy of the total of  $M$  eddies encountered by the DH within the resolution volume centered at the range  $r_0$ .

The range-weighting function  $W_r$  represents the convolution between the impulse response of the receiver with the transmitted pulse and is described by Holdsworth and Reid (1995) and Scipión et al. (2008) as

$$W_r^{(m)} = \exp \left[ -\frac{(r^{(m)} - r_0)^2}{2\sigma_r^2} \right], \quad (19)$$

where  $r^{(m)}$  represents range of the  $m$  eddy and  $\sigma_r = 0.35c\tau_w/2$ .

### 3 Experimental setup

#### 3.1 Site description

The SOUSY radar is installed at JRO, located at 511 m above sea level approximately 25 km from the city of Lima, Peru. The location of the DataHawk launch site was approximately at 0.8 km northeast from the SOUSY radar because it is both close to the radar site and far away from possible sources of interference during preflight calibration. See Fig. 1.

#### 3.2 SOUSY radar

The SOUSY radar was donated by the Max-Planck-Institut für Aeronomie to the Instituto Geofísico del Perú in 2000 (Woodman et al., 2003) and installed at JRO to complement JRO studies due to SOUSY's large bandwidth (4 MHz compared to 700 kHz from the Jicamarca radar), which provides atmospheric measurements with high spatial resolution (37.5 m). SOUSY specifications and parameters are presented in Table 1.

Shortly after its installation at Jicamarca, a new digital acquisition system was developed using an off-the-shelf AD6620 digital receiver board to take full advantage of SOUSY's wide bandwidth (Woodman et al., 2003; Alcantara and Abad, 2008). For the upgrade to be fully functional, it included a radar controller and direct digital synthesizer.

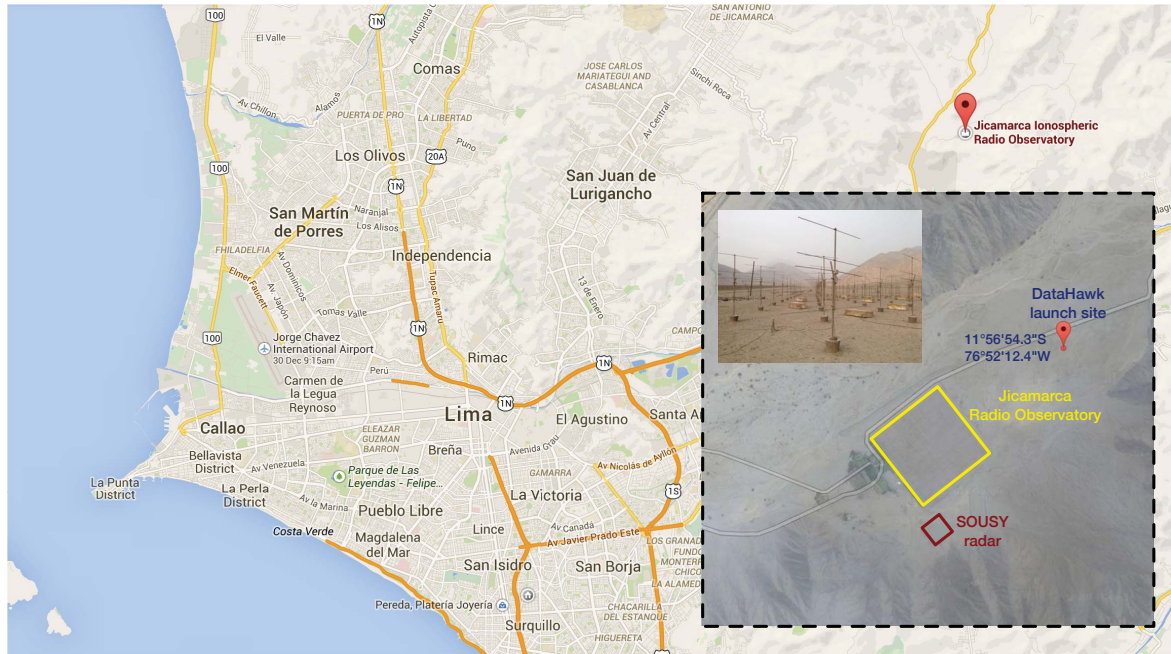


**Figure 1.** The Jicamarca Radio Observatory (JRO) is the experimental site for the observational campaign. JRO is located approximately 25 km from the city of Lima. The DataHawk launch site is on the JRO property 400 m from the main antenna (marked in yellow). The SOUSY radar is located next to the main antenna (marked in red). A picture of the SOUSY antenna elements is presented in the top left corner of the dash rectangle.

**Table 1.** SOUSY radar specifications.

Quantity	Value
Radar type	Pulsed
Frequency	53.5 MHz
Wavelength	5.6 m
Beamwidth	~ 4.9°
Bandwidth	4 MHz
Transmitter peak power	20 kW
Receiver	Digital based on AD6620 chip
Processing type	Spectra
Number of FFT points	8
Number of coherent integrations	4096
Number of incoherent integrations	1
Dwell time	12.5 s
Unambiguous velocity	1.1 m s <sup>-1</sup>
Mode 1	Characteristics
Inter pulse period (IPP)	57.2062 km
Pulse width	300 m
Code	Complementary 8 baud
Range resolution	37.5 m
Duty cycle	0.5244%
Mode 2	Characteristics
Inter pulse period (IPP)	57.2062 km
Pulse width	37.5 m
Code	None
Range resolution	37.5 m
Duty cycle	0.0655 %

Initial results confirmed SOUSY’s ability to provide high range resolution, which proves that it is a valuable tool with which to study the morphology of turbulent layers under statistically stable stratified conditions (Woodman et al., 2007). During the present campaign the beam was set to point vertically, to be coincident with vertical DataHawk helix profiles.

### 3.3 DataHawk

The DataHawk is a sUAS that was specifically designed for high-resolution, multiple-variable, state-of-the-art atmospheric sensing measurements (Lawrence and Balsley, 2013a). The atmospheric regions targeted by the DataHawk are the atmospheric boundary layer (ABL) and lower troposphere (up to 10 km).

The maximum altitude reached by the DH depends on the launch method: when launched from the ground (bungee launch), it can reach up to 2.5 km at a 2 m s<sup>-1</sup> rise rate. Higher altitudes (up to 10 km) can be reached when it is launched by a balloon drop (see Fig. 2a), in which the DH detaches at a prescribed altitude and then flies back upwind to the desired region (Fig. 2b). Upon reaching the study region, the DH descends (or ascends depending on the launch method) in a helix trajectory as shown in Fig. 2c. A detailed list of the capabilities, sensors, and system characteristics of the DataHawk is provided in Table 2.

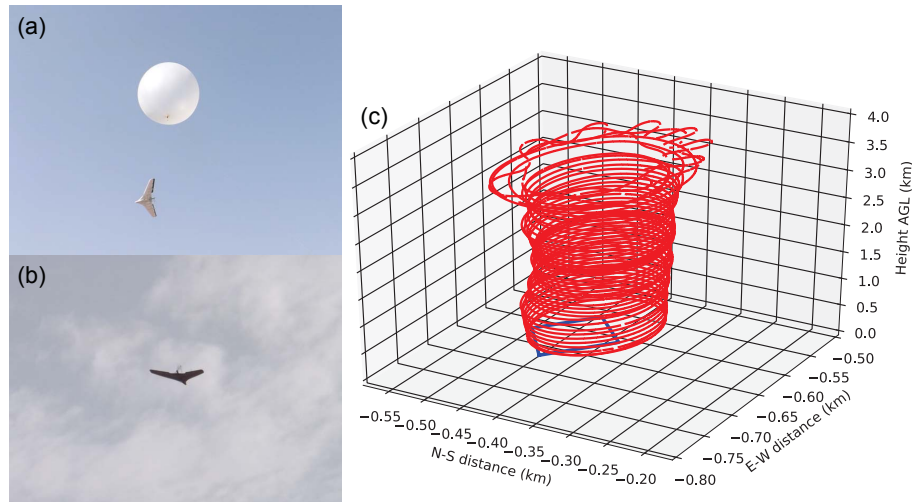


**Figure 2.** (a) Balloon lifting the DataHawk for the afternoon data set on 10 July 2014. (b) DataHawk flying towards the landing site for the same data set at an approximate altitude of 50 m. (c) Helical trajectory of the DataHawk descending from approximately 3.75 km to 500 m over the SOUSY radar (indicated in blue).

**Table 2.** DataHawk sensing system characteristics and capabilities (extracted from Lawrence and Balsley, 2013a).

	Value		Value
Wingspan	1 m	Alt. (balloon drop)	> 9 km m.s.l.
Mass	0.7 kg	Alt. (bungee launch)	> 2 km a.g.l.
Design	Flying wing, rear propeller	Turning radius	> 50 m
Telemetry	IEEE 802.15.4 at 2.4 GHz	Climb rate	< 5 m s <sup>-1</sup>
Propulsion	Electric motor, folding propeller	Downlink throughput	> 1500 bytes s <sup>-1</sup>
Autopilot	CU custom design (CUPIC)	Downlink update rate	10 Hz
Control	Auto-helix, balloon drop	Sensor sampling	> 100 Hz
Power	11-V LiPo battery, 2600 mA h <sup>-1</sup>	Data storage (on board)	16 MB

Sensing capabilities				
Type	Resolution	Accuracy; range	Time const.; cadence	Notes
Location (GPS)	0.1 m	10 m; worldwide	1 s; 4 Hz	Real time
In situ temperature	0.1 °C	2 °C; -60 to +40°	5 s; 8.1 Hz	Real time
Relative humidity	0.01 %	2 %; 0–100 %	5 s; 8.1 Hz	Real time
Cold-wire temperature	< 0.003 °C	2 °C; -60 to +40 °C	0.5 ms; 81 Hz	Real time; postflight calibration
Airspeed	0.01 m s <sup>-1</sup>	0.2 m s <sup>-1</sup> ; 0–30 m s <sup>-1</sup>	0.3 ms; 81 Hz	Real time

**Table 3.** SOUSY and DataHawk coordinated events.

Date	Period	Max. Altitude	Radar Mode
10 July 2014	11:05–11:30 UTC-5	2800 m	Mode 2
10 July 2014	15:21–15:46 UTC-5	3850 m	Mode 1

## 4 Results

A campaign for coordinated observations using the DataHawk and the SOUSY radar was conducted between 5 and 10 July 2014. The first few days were used to set up the in-

struments, test launch and recovery at the site, and conduct test flights. The main observations were made on 10 July 2014. There were two flights that reached the desired altitude within the radar beam (see Table 3).

Two radar pulse configurations were tested with SOUSY and are outlined in Table 1. The main difference between the two modes is the average transmitted power: mode 1 transmits 8 times the power of mode 2 and uses pulse compression to keep the same range resolution.

Radar returns for 10 July 2014 between 09:10 and 17:30 LT are presented in Fig. 3. Data between 09:10 and 13:50 were acquired using mode 2, while data between 14:40

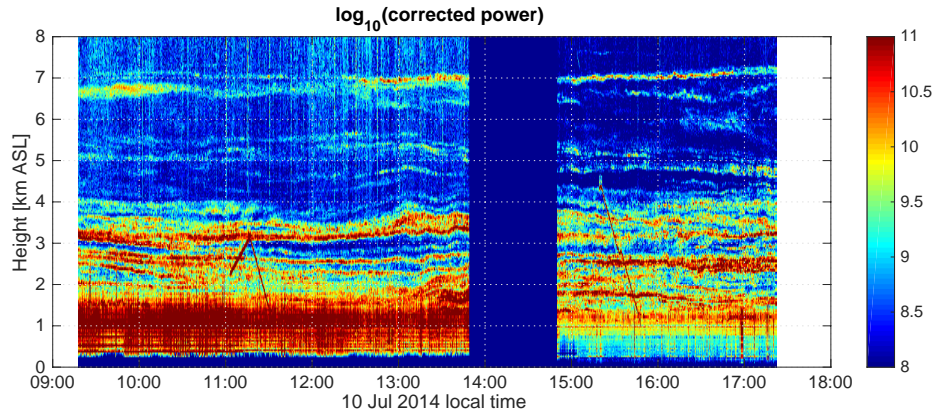


**Figure 3.** SOUSY daytime calibrated range-corrected received power for 10 July 2014 shows distinct turbulent layers from 500 m up to 7 km. The dropout of data between 14:00 and 15:00 was due to upgrades in the radar system that allowed for discrimination of echo returns below 1 km. DataHawk flights over the radar were easily detected as an increase of the radar returns between 11:05 and 11:30 and between 15:21 and 15:46.

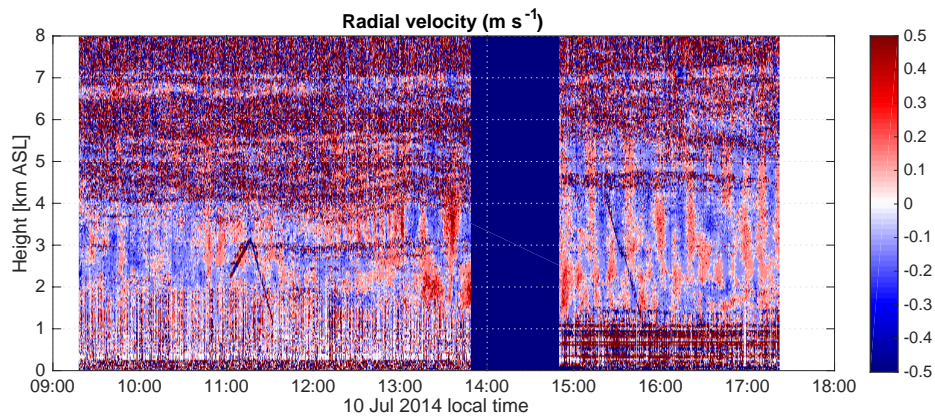


**Figure 4.** Daytime vertical velocity for 10 July 2014 shows stratified layers in the morning evolving into updrafts and downdrafts in the afternoon with a periodicity of approximately 10 min. The propagation of the updrafts reached altitudes close to 7 km.

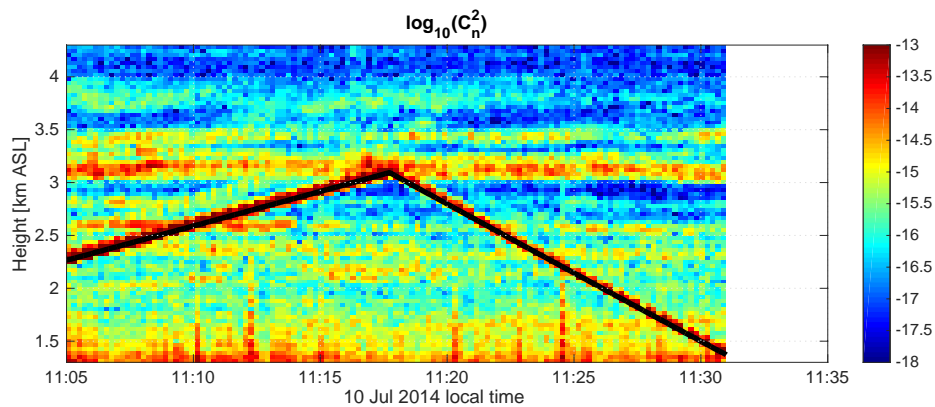


**Figure 5.** The black line represents the DataHawk altitude as a function of time plotted on top of the calibrated range-corrected received power for the morning flight (11:05–11:30). The DataHawk was dropped by a tethered balloon at an approximate altitude of 2.25 km. In this case, there is an ascent from its initial altitude to 3 km, followed by a descent over SOUSY down to 1.5 km.

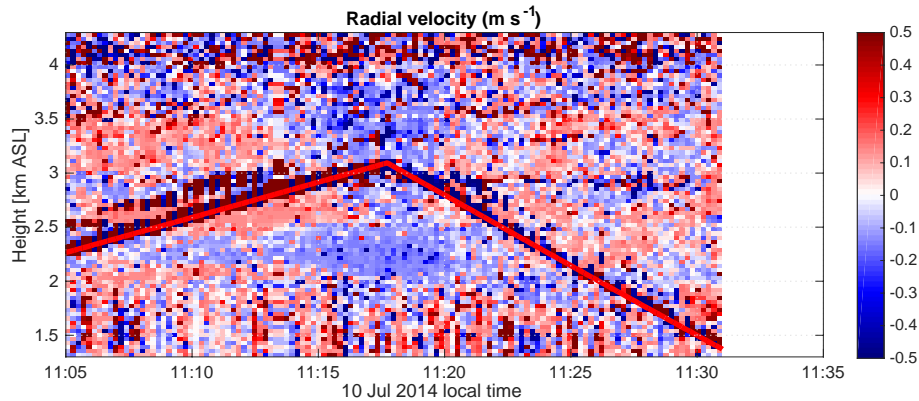


**Figure 6.** Corresponding radial velocity for the morning flight (same period as Fig. 5). The DataHawk trajectory is indicated by the red line. Vertical wind cannot be determined by the radar along the DH path due to strong returns from the DH vehicle.

and 17:30 were acquired using mode 1. The gap observed between 13:50 and 14:40 was due to a change in the  $T/R$  switch. This change gave a better recovery time of the signal, which allowed the detection of layers down to 500 m range, in comparison with the old design that only allowed discrimination of turbulent layers from ranges above 1.2 km. For better comparison of both modes, the power is corrected by range and the difference in the average transmitted power.

Different layers are clearly observed throughout the day especially between 2 and 4 km (see Fig. 3), which shows SOUSY's potential for turbulence studies. Both DH flights over SOUSY are seen in the radar data as straight lines relating altitude and time, with an increase in the returned power (see the saturated red lines between 11:05 and 11:30, and between 15:20 and 15:45). In addition to the increase in the returned power from DataHawk reflections, the vertical velocity signatures of the DH flights can be observed in Fig. 4. The evolution of the updrafts and downdrafts throughout the day and their propagation to altitudes up to 6.5 km can also be observed.

#### 4.1 Results from 10 July 2014, flight starting at 10:03:46 LT

The morning flight over the SOUSY radar was a balloon drop using a tethered balloon that reached approximately 2 km altitude from the launch site. Right after the drop, the DH flew over the SOUSY radar and started its spiral ascent up to 2.8 km, which was limited because of battery life. After reaching its maximum altitude, it descended down to 500 m and returned to the launch site for landing. The total time of the flight over SOUSY was approximately 25 min. A close-up of the calibrated range-corrected received power is presented in Fig. 5. The black line presented on top of the radar data represents the altitude measured directly by a pressure sensor on the DataHawk. Not only can the DH ascent and descent be clearly observed in the radar data, but the agreement

in time and altitude between these instruments is within the resolution of the data (37.5 m in altitude, 12.5 s in time).

Estimations of  $C_n^2$  (DH direct) along the helical path were calculated by first calculating  $N$  at each of the measured points (see black dots in Fig. 8) and then calculating  $\delta_E$  for each of the measured points (see red thick line in Fig. 8) after correcting for advection. The horizontal winds  $u$  and  $v$  were obtained from the DH (Lawrence and Balsley, 2013b) and are presented in Fig. 7. The vertical wind  $w$  was measured directly from the radar and is presented in Fig. 6. However, due to the strong return signal caused by the DH as seen by the radar, estimates of  $w$  were clearly contaminated, and it was impossible to retrieve these estimates at the exact altitude of the DH. However, their values at other altitudes were bounded by  $[-0.4, 0.4]$   $\text{m s}^{-1}$  and will be neglected in the calculations of  $\delta_E$ . Estimates of  $C_n^2$  were obtained at Bragg scale (2.8 m), but their contributions were integrated over the radar resolution (37.5 m).

A second method to estimate  $C_n^2$  (DH ISR) that follows the modifications discussed earlier of the method of Wainwright et al. (2015) and Bonin et al. (2015) was implemented only for the ascent part of the trajectory. Reflectivity  $N$  was divided into small portions of 18.75 m that contained at least one half rotation on the helix trajectory to reduce the contribution of vertical variability of  $N$ .

A sample of the  $N$  portion centered at 2362.50 m is presented in Fig. 9a. The variability of  $N$  ( $\delta N$ ) with respect to the set of  $\delta_E$  is presented in Fig. 9b, where the bias caused by the vertical variability of  $N$  can be clearly observed, as the distribution shifts to negative values while  $\delta_E$  increases.  $D_n$  or  $\overline{(\delta n)^2}$  is instead calculated as the variance of  $(\delta N)$  at each 10 m bin and presented in Fig. 9c. The use of the variance removes the mean of the bias observed in the calculations. Finally, estimates of  $C_n^2$  for each  $\delta_E$  are presented in Fig. 9d. From inspection the ISR, where  $C_n^2$  is constant and independent of  $\delta_E$ , is bounded between 60 and 100 m.

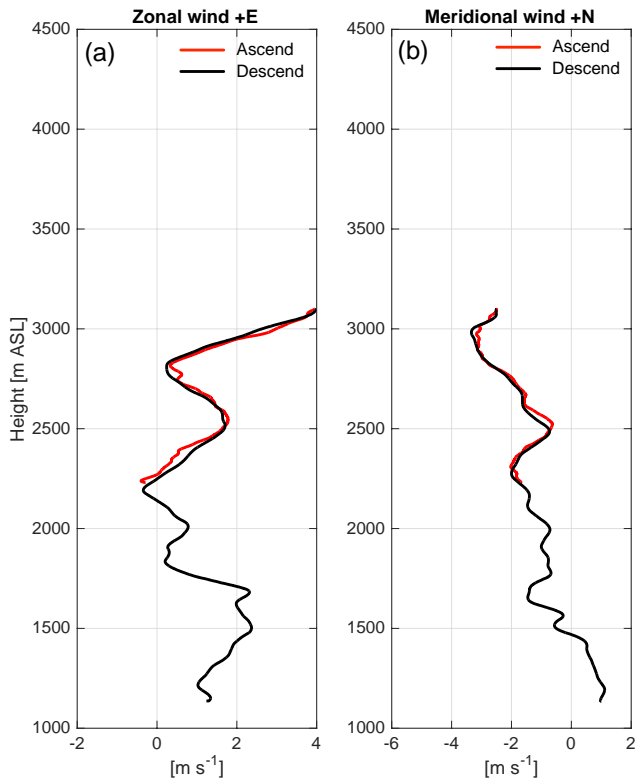


**Figure 7.** Horizontal winds obtained from the DataHawk for the morning flight. (a) Zonal wind. (b) Meridional wind. The red line indicates the ascent portion of the flight, while the black line indicates the descent portion of the flight.

Estimation of  $C_n^2$  from the two instruments is presented in Fig. 10. Estimates from ascending and descending flights are presented in Fig. 10a and Fig. 10b, respectively. In both figures, instantaneous  $C_n^2$  estimated profiles obtained from the radar are presented in thin light-gray lines, one for every dwell time (12.5 s) over the time period corresponding to the colocated DH flight. All these radar estimates of  $C_n^2$  have the segments of increased power from the DH reflections removed. The time average of these radar instantaneous profiles at each altitude is presented as the thick dark-gray line, exhibiting rather stationary gross features over this time period but with significant variability in the details of the profiles over time.

In contrast, the DataHawk measurements are not averaged over this 25 min interval but are instantaneous at a given altitude and time. So a more direct comparison would be obtained by extracting the radar returns at the altitude and time occupied by the DataHawk. As the DataHawk itself obliterates the radar returns there, due to its larger reflectivity, the next-best comparison is to use an average of the radar returns just before and after the DataHawk reflection. This is presented by the thick black line.

Turbulent layers are identified by a relative increase in the  $C_n^2$  values at those altitudes. The agreement between

the directly corresponding measurements (DH direct – red; SOUSY – black) is remarkable, especially during the ascent portion of the morning flight and above 1.75 km in the descent portion, where the radar data not only agree with the DH data in magnitude of  $C_n^2$  but clearly follow each other in all the main layered features. Below 1.75 km on the descent the main variations becomes smaller, and the degree of detailed correspondence between the red and blue lines breaks down, although the averages over altitude continue to track well. The order of magnitude of  $C_n^2$  profiles in these data is consistent with experimental observations (Van Zandt et al., 1978; Gage et al., 1980), and according to a category defined by Davis (1966), the level of turbulence varies from intermediate to moderate.

Comparisons of  $C_n^2$  obtained from the DH ISR estimate (blue) and the other estimates are only presented for the ascent part (Fig. 10a). The agreement is observed above 2.5 km, where all the estimates have the same order of magnitude. Possible causes for the overestimation of DH ISR below 2.5 km are, first, vertical variability of the refractive index (clearly observed in Fig. 9b). Second, the identified inertial subrange lies at separations higher than the Bragg scale (2.8 m) in Fig. 9d. Third, the radar Bragg scale is only represented by the first point in Fig. 9d, which clearly misrepresents the radar measure of turbulence. Finally, we consider the DH direct method to be the best way to capture the turbulence at the radar Bragg scale.

The DH ISR method was not implemented in the descent portion due to the higher descent rate ( $2 \text{ m s}^{-1}$ ), which will increase the size of the portion that will complete the half helix, thereby increasing the vertical variability of the refractive index.

#### 4.2 Results from 10 July 2014, DH flight starting at 14:42:12

The afternoon DH flight was a balloon drop from an altitude of 6.7 km, several kilometers south of the SOUSY radar. At approximately 4 km during the descent the DH arrived over the radar and started the helical descent at  $2 \text{ m s}^{-1}$ , continuing down to an altitude of 600 m before returning to the launch site. The calibrated radar returns during the flight are presented in Fig. 11, while the radial velocities are presented in Fig. 12. Note the small kink in the descent trajectory where the DH was inadvertently commanded to climb for a short period. Again the similarities in the altitudes of both trajectories (obtained from DH and detected by SOUSY) are excellent. As in the previous case, comparisons of  $C_n^2$  were computed for both DH and SOUSY, and are presented in Fig. 14. Again the  $\delta_E$  was corrected for advection with zonal and meridional winds presented in Fig. 13, and the vertical velocity was neglected. For this case, there is only a descending flight over the radar, beginning at an altitude of  $\sim 4.2$  km. The location of the turbulent layers and their morphology are

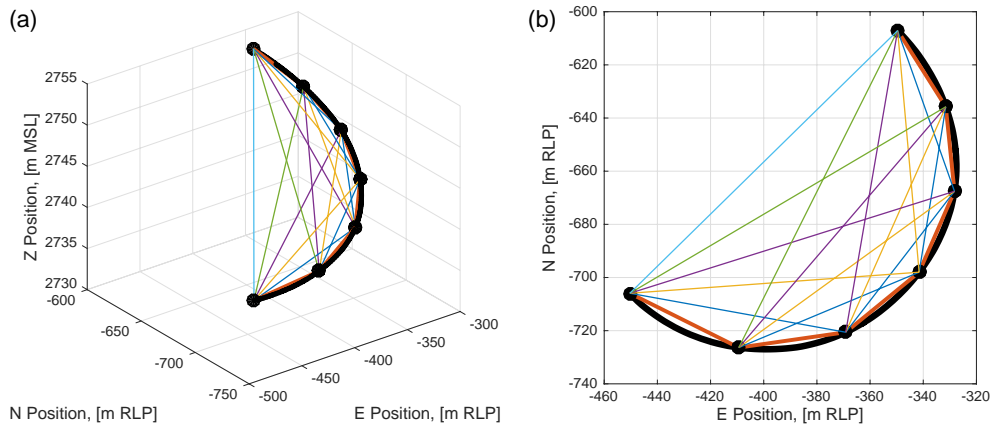


**Figure 8.** Illustration of a method for evaluating  $C_n^2$  (adapted from Wainwright et al., 2015; Bonin et al., 2015) for a helical trajectory. The different distances  $\delta_E$  are represented by the lines with different colors. The measured points are indicated by the black dots. The smallest distance used in the DH direct method is indicated by the thick red line. (a) 3-D view of the trajectory for a portion that covers at least one half circle. (b) Top view of the trajectory.

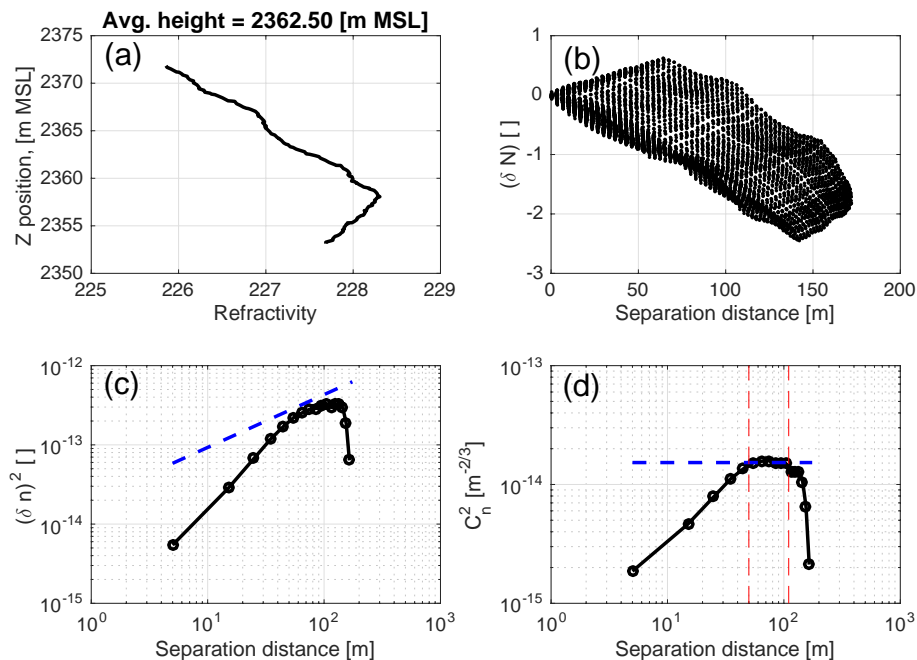


**Figure 9.** Procedure followed for the evaluation of  $C_n^2$  in the inertial subrange (ISR) for the portion of the ascent trajectory similar to the one presented in Fig. 8. (a) Refractivity as a function of height that corresponds to an average height of 2362.50 m with a span of 18.75 m. (b) Variations for  $\delta N$  with separation distance. Data clearly present a bias due to the helical (non-flat) trajectory. (c) Variations of  $(\delta n)^2$  with separation evaluated with 10 m bin. (d) Variation of  $C_n^2$  with distance. The red lines mark the bounds of the ISR, where the turbulence is constant and independent of  $\delta_E$ , and the blue line is the corresponding  $C_n^2$  value.

similar from both SOUSY and the DH data for the DH direct method to those in the morning flight.

### 4.3 Radar calibration constant

In each of the two cases above, the radar returns were calibrated by applying the appropriate calibration constant  $C$  to bring the DH and SOUSY  $C_n^2$  estimates into general agree-

ment. If this constant takes into account all the major factors, and the theory is adequate to describe the general conditions of interest, then this one constant should provide a correspondence that holds up over time and over variations in conditions within those of interest. Finally, introducing the different parameters in Eq. (17), the “best” value of the calibration constant  $C$  for the morning flight in the data shown above

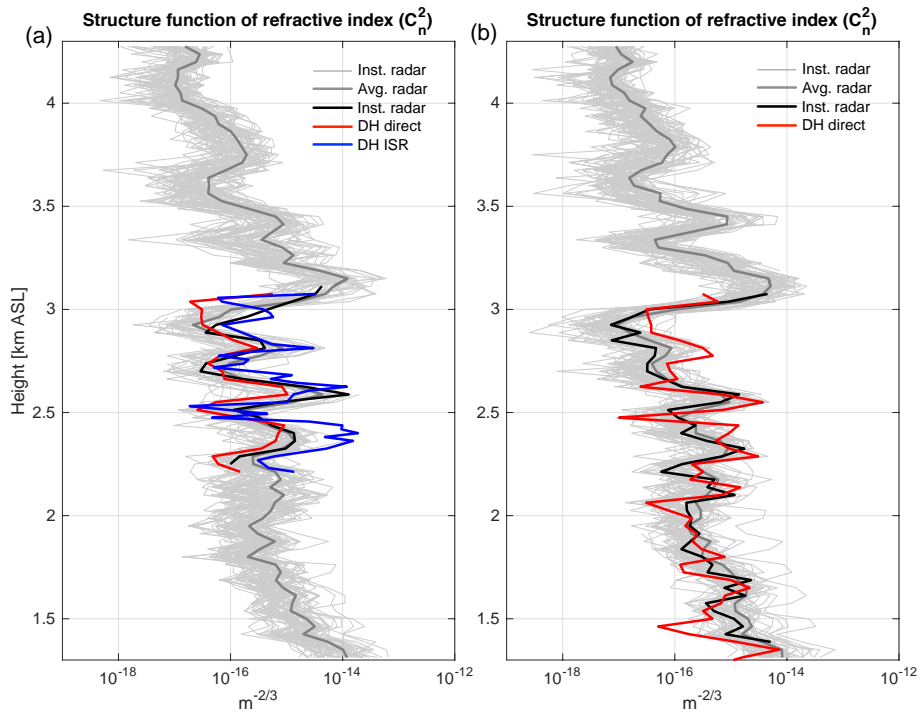


**Figure 10.** Structure parameter of refractive index obtained during the ascent (a) and descent (b) portions of the morning flight over the SOUSY radar. The light-gray lines represent the multiple  $C_n^2$  profiles obtained from SOUSY for the corresponding flight. The thick dark-gray line is the radar average over the same period. The thick black line represents the  $C_n^2$  obtained from the radar around the closest times after the DH signature is removed. The thick red line represents  $C_n^2$  obtained from the DataHawk estimated for a distance corresponding to the Bragg scale ( $\lambda_B = 2.8$  m). Finally, the thick blue line represents  $C_n^2$  estimated within the ISR but only estimated for the ascent portion of the flight.

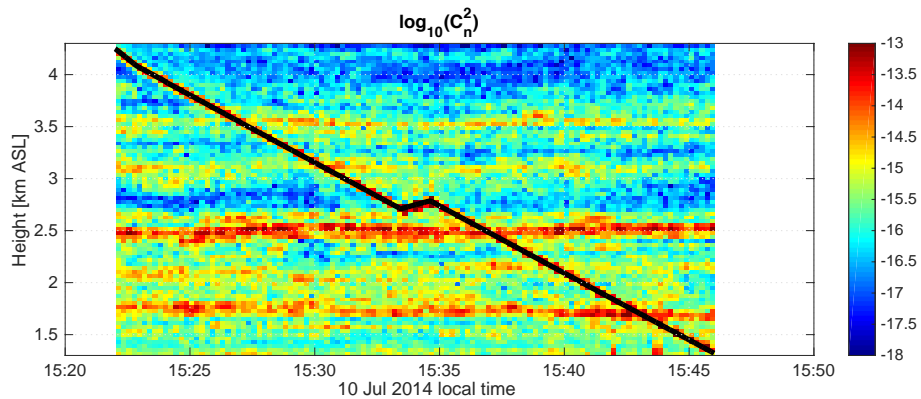


**Figure 11.** Similar to Fig. 5 but during the afternoon flight (15:21–15:46). In this case, the DataHawk was dropped by a “free” balloon at an altitude of approximately 8 km. However, due to the strong winds, the DataHawk was advected 4 km from the SOUSY radar, which caused a 3 km drop during the time it took to regain its position over the radar.

was  $6 \times 10^{-26} \text{ m}^{-5/2} \text{ mW}^{-1}$  and  $7 \times 10^{-26} \text{ m}^{-5/2} \text{ mW}^{-1}$  for the afternoon flight. The small discrepancies observed in the calibration constant for both flights might be caused by the change in the  $T/R$  switch, which might have introduced a change in the sensitivity in the returned signal, and by the peak transmitted power, which might not have remained constant due to changes in the operational modes.

After combining both (morning and afternoon) estimates,  $C = 6.5 \times 10^{-24} \text{ m}^{-5/2} \text{ mW}^{-1}$  was estimated for the whole day.

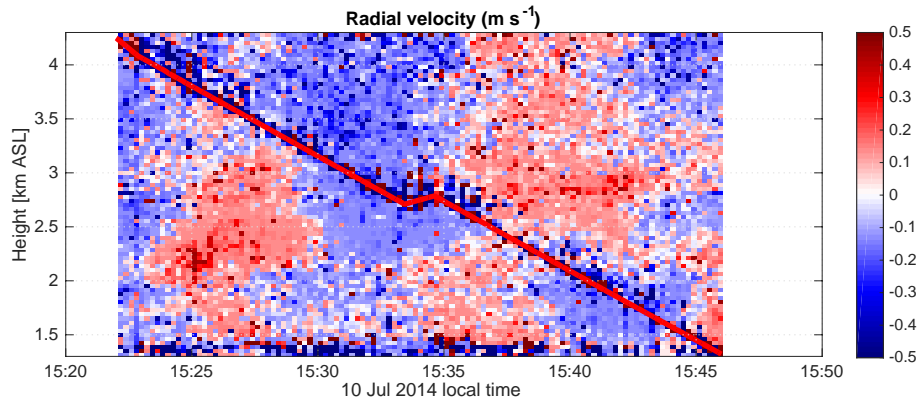


**Figure 12.** Similar to Fig. 6 but for the afternoon flight. Estimates of the vertical wind cannot be estimated from radar returns along the DataHawk path due to its high reflectivity.

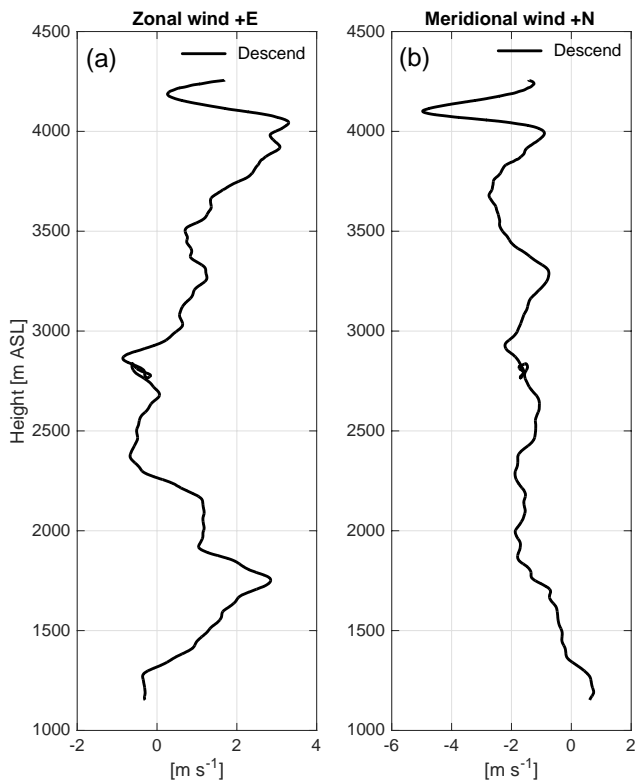


**Figure 13.** Horizontal winds for the afternoon flight (15:21–15:46) estimated from the DataHawk. (a) Zonal wind. (b) Meridional wind.

## 5 Conclusions and future work

Radar profiling of atmospheric turbulence and associated fine-structure atmosphere has the potential to unravel important details of mixing and transport processes, owing to its instantaneous profiling capabilities near the boundary layer up into the stratosphere and its ability to provide continuous measurements over extended periods. Unfortunately, radar

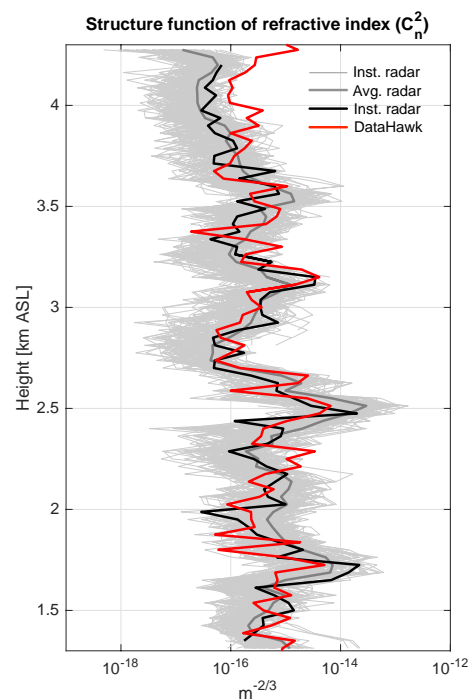


**Figure 14.** Similar to Fig. 8 but during the afternoon flight (15:21–15:46), which only had a descent trajectory.

return power is a complex function of difficult-to-measure radar parameters and various turbulent atmospheric scattering phenomena.

This paper showed how the measurement of the turbulent structure function parameter of refractive index  $C_n^2$  obtained from the radar can be calibrated using a small unmanned aircraft system (the DataHawk) to provide coincident in situ measurements inside the radar beam. This one-time calibration enables the radar to provide quantitative estimates of this turbulence parameter continuously thereafter, in turn en-

abling more detailed studies of these structures and their evolution.

Since turbulence can have a complex and evolving character, radar returns alone, by their dependence on refractive index alone, are not likely to suffice for study of turbulence processes in general, without information from other sources. Accordingly, future work will include periodic observational campaigns (every 3 months) that will include the DataHawk, SOUSY, and probably additional radars. A different flight trajectory should be tested in order to account for only the horizontal variations of the refractive index  $n$  at different heights. These campaigns will seek to add estimates of the structure parameters of temperature  $C_T^2$  and turbulent energy dissipation rates  $\epsilon$ . Another addition might be the recently installed Advanced Modular Incoherent Scatter Radar (AMISR) at JRO that operates at 450 MHz. AMISR has a pulse-to-pulse beam steer capability that could allow us to compare and validate horizontal wind estimates obtained from the DataHawk.

## 6 Data availability

Data are available from <http://sic.igp.gob.pe/webshared/index.php/s/HhhWceGHfMfTmrt> (Scipi3n et al., 2016).

Two directories are available: one from the SOUSY radar and the other from the DataHawk. The data are recorded as an output matlab file “.mat”.

*Acknowledgements.* Thanks to all Jicamarca staff for their help with operation of SOUSY during this campaign and especially to those who helped with the DataHawk balloon drop operations at JRO and the University of Colorado. This research is partially by NSF (1041963) and ARO (W911NF-12-2-0075), whose support is gratefully acknowledged. The Jicamarca Radio Observatory is a facility of the Instituto Geofisico del Per3u operated with support from the NSF AGS-1433968 through Cornell University.

The topical editor, M. Salzmann, thanks three anonymous referees for help in evaluating this paper.

## References

- Alcantara, J. and Abad, R.: Sistema de Adquisici3n utilizando receptores digitales. Proyecto REX-2X, Informe t3cnico, Instituto Geofisico del Per3u, 2008.
- Balsley, B. B., Lawrence, D. A., Woodman, R. F., and Fritts, D. C.: Fine-scale characteristics of temperature, winds, and turbulence in the lower atmosphere (0–1300 m) over the south Peruvian coast, *Bound.-Lay Meteorol.*, 147, 165–178, doi:10.1007/s10546-012-9774-x, 2012.
- Bean, B. R. and Dutton, E. J.: *Radio Meteorology*, vol. 92 of Natl. Bur. Stand. Monogr., Supt. Doc. U.S. Govt. Printing Office, Washington D.C., USA, 1966.
- Bonin, T. A., Goines, D. C., Scott, A. K., Wainwright, C. E., Gibbs, J. A., and Chilson, P. B.: Measurements of temperature

structure-function parameters with a small unmanned aerial system compared with a sodar, *Bound.-Lay. Meteorol.*, 155, 417–434, doi:10.1007/s10546-015-0009-9, 2015.

- Cho, J. Y. N., Jurgens, R. F., and Slade, M. A.: High-resolution stratospheric dynamics measurements with the NASA/JPL Goldstone Solar System Radar, *Geophys. Res. Lett.*, 23, 1909–1912, 1996.
- Cohn, S. A.: Radar measurements of turbulent eddy dissipation rate in the troposphere: A comparison of techniques, *J. Atmos. Ocean. Tech.*, 12, 85–95, 1995.
- Czechowsky, P., Klostermeyer, J., R3ttger, J., R3ster, R., Schmidt, G., and Woodman, R. F.: The SOUSY-VHF-radar for tropospheric, stratospheric, and mesospheric sounding, in: *Preprints, 17th Radar Meteorology Conf.*, Seattle, WA, USA, Amer. Meteor. Soc., 349–353, 1976.
- Davis, J. I.: Consideration of atmospheric turbulence in laser system design, *Appl. Optics*, 5, 139–147, 1966.
- Doviak, R. and Zrni3, D. S.: Reflection and scatter formula for anisotropically turbulent air, *Radio Sci.*, 19, 325–336, 1984.
- Doviak, R. J. and Zrni3, D. S.: *Doppler Radar and Weather Observations*, Academic Press, San Diego, CA, USA, 2nd edn., 1993.
- Gage, K. S., Green, J. L., and Van Zandt, T. E.: Use of Doppler radars for the measurement of atmospheric turbulence parameters for the intensity of clear-air echoes, *Radio Sci.*, 15, 407–416, 1980.
- Hocking, W. K.: Measurement of turbulent eddy dissipation rates in the middle atmosphere by radar techniques: A review, *Radio Sci.*, 20, 1403–1422, 1985.
- Hocking, W. K.: An assessment of the capabilities and limitations of radars in measurements of upper atmospheric turbulence, *Adv. Space Res.*, 17, 37–47, 1996.
- Hocking, W. K. and Mu, P. K. L.: Upper and middle tropospheric kinetic energy dissipation rates from measurements of  $C_n^2$  – review of theories, in-situ investigations, and experimental studies using the Buckland Park atmospheric radar in Australia, *J. Atmos. Sol.-Terr. Phys.*, 59, 1779–1803, 1997.
- Hocking, W. K., Hocking, A., Hocking, D. G., and Garbanzo-Salas, M.: Windprofiler optimization using digital deconvolution procedures, *J. Atmos. Sol.-Terr. Phys.*, 118, 45–54, doi:10.1016/j.jastp.2013.08.025, 2014.
- Holdsworth, D. A. and Reid, I. M.: A simple model of atmospheric radar backscatter: Description and application to the full correlation analysis of spaced antenna data, *Radio Sci.*, 30, 1263–1280, 1995.
- Holton, J. R.: *An Introduction to Dynamic Meteorology*, vol. 88 of International Geophysics Series, Elsevier Academic Press, Burlington, MA, USA, 4th edn., 2004.
- Kolmogorov, A. N.: The local structure of turbulence in incompressible viscous fluid for very large Reynolds numbers, *Dokl. Akad. Nauk SSSR+*, 30, 299–303, 1941.
- Lawrence, D. A. and Balsley, B. B.: High-resolution atmospheric sensing of multiple atmospheric variables using the DataHawk small airborne measurement system, *J. Atmos. Ocean. Tech.*, 30, 2352–2366. doi:10.1175/JTECH-D-12-00089.1, 2013a.
- Lawrence, D. A. and Balsley, B. B.: Design of low-cost UAS for high resolution atmospheric sensing, in: *Proc. AIAA Infotech@Aerospace conference*, Boston, MA, USA, 2013b.

- Luce, H., Crochet, M., Dalaudier, F., and Sidi, C.: Interpretation of VHF ST radar vertical echoes from in situ temperature sheet observations, *Radio Sci.*, 30, 1002–1025, 1995.
- Luce, H., Fukao, S., Dalaudier, F., and Crochet, M.: Strong Mixing Events Observed near the Tropopause with the MU Radar and High-Resolution Balloon Techniques, *J. Atmos. Sci.*, 59, 2885–2896, 2002.
- Luce, H., Hassenpflug, G., Yamamoto, M., and Fukao, S.: Comparisons of refractive index gradient and stability profiles measured by balloons and the MU radar at a high vertical resolution in the lower stratosphere, *Ann. Geophys.*, 25, 47–57, doi:10.5194/angeo-25-47-2007, 2007.
- Ottersten, H.: Mean vertical gradient of potential refractive index in turbulent mixing and radar detection of CAT, *Radio Sci.*, 4, 1247–1249, 1969a.
- Ottersten, H.: Radar backscattering of the turbulent clear atmosphere, *Radio Sci.*, 4, 1251–1255, 1969b.
- Ottersten, H.: Atmospheric structure and radar backscattering in clear air, *Radio Sci.*, 4, 1179–1193, 1969c.
- Richardson, L. F.: *Weather prediction by numerical process*, Cambridge University Press, Cambridge, UK, 1st edn., 1922.
- Richter, J. H.: High resolution tropospheric radar sounding, *Radio Sci.*, 4, 1261–1268, 1969.
- Rogers, R. R. and Yau, M. K.: A short course in cloud physics, vol. 113 of International series in natural philosophy, Butterworth Heinemann, Burlington, MA, USA, 3rd edn., 1989.
- Röttger, J. and Larsen, M. F.: UHF/VHF radar techniques for atmospheric research and wind profiler applications, in: *Radar in Meteorology*, edited by: Atlas, D., American Metr. Soc, Boston, MA, USA, 235–286, 1990.
- Röttger, J. and Schmidt, G.: High-resolution VHF radar sounding of the troposphere and stratosphere, *IEEE T. Geosci. Elect.*, GE-14, 182–189, 1979.
- Rüster, R., Klostermeyer, J., and Röttger, J.: SOUSY VHF radar measurements in the lower and middle atmosphere, *IEEE T. Geosci. Remote*, GE-24, 966–974, 1986.
- Scipión, D. E., Chilson, P. B., Fedorovich, E., and Palmer, R. D.: Evaluation of an LES-based Wind Profiler Simulator for Observations of a Daytime Atmospheric Convective Boundary Layer, *J. Atmos. Ocean. Tech.*, 25, 1423–1436, doi:10.1175/2007JTECHA970.1, 2008.
- Scipión, D. E., Lawrence, D. A., Woodman, R. F., Lume, D. A., Milla, M. A., and Balsley, B. B.: DataHawk and SOUSY measurements, available at: <http://sic.igp.gob.pe/webshared/index.php/s/HhhWceGHfMfTmrt>, last access: September 2016.
- Skolnik, M. I.: *Radar Handbook*, McGraw-Hill, New York, USA, 2nd edn., 1990.
- Tatarskii, V. I.: *Wave Propagation in a Turbulent Medium*, McGraw-Hill, New York, USA, 1961.
- Tatarskii, V. I.: *The effects of turbulent atmosphere on wave propagation*, Israel Program for Scientific Translations, Jerusalem, 1971.
- Taylor, G. I.: The spectrum turbulence, *P. R. Soc.*, 164, 476–490, 1938.
- Van Zandt, T. E., Green, J. L., Gage, K. S., and Clark, W. L.: Vertical profiles of reflectivity turbulence structure constant: Comparison of observations by the Sunset radar with a new theoretical model, *Radio Sci.*, 13, 819–829, 1978.
- Wainwright, C. E., Bonin, T. A., Chilson, P. B., Gibbs, J. A., Fedorovich, E., and Palmer, R. D.: Methods for evaluating the temperature structure-function parameter using unmanned aerial system and large-eddy simulations, *Bound.-Lay Meteorol.*, 155, 189–208, doi:10.1007/s10546-014-0001-9, 2015.
- White, A. B.: Radar remote sensing of scalar and velocity micro-turbulence in the convective boundary layer, NOAA Technical Memorandum ERL ETL-276, Environmental Research Laboratories, Boulder, CO, USA, 1997.
- Woodman, R., Castillo, O., Michhue, G., Reyes, P., and Villegas, S.: SOUSY radar at Jicamarca: System Description, in: *Extended Abstracts: 10th International Workshop on Technical and Scientific Aspects of MST Radar*, Piura, Peru, available at: [http://jro.igp.gob.pe/mst10/CD/ExtAbs/Session5/I5\\_518.pdf](http://jro.igp.gob.pe/mst10/CD/ExtAbs/Session5/I5_518.pdf) (last access: September 2016), 2003.
- Woodman, R., Michhue, G., Röttger, J., and Castillo, O.: The MPI-SOUSY-VHF radar at Jicamarca: High Altitude-Resolution Capabilities, in: *Extended Abstracts: 11th International Workshop on Technical and Scientific Aspects of MST Radar*, Gadanki, India, available at: <http://www.igp.gob.pe/descargas/ronw/SOUSY/TheMPIOusyRadaratJicamarcaextendedabstract.pdf> (last access: September 2016), 2007.
- Woodman, R. F. and Guillen, A.: Radar observations of winds and turbulence in the stratosphere and mesosphere, *J. Atmos. Sci.*, 31, 493–505, 1974.